Spectroscopic Study of Molybdenum Impurity Generation in LHW Sustained Plasmas on TST-2 Spherical Tokamak

Yiming TIAN, Akira EJIRI, Naoto TSUJII, Yuting LIN, Kouji SHINOHARA, Seowon JANG, Yi PENG, Kotaro IWASAKI and Fumiya ADACHI

Graduate School of Frontier Sciences, The University of Tokyo, Kashiwa 277-8561, Japan

(Received 30 November 2023 / Accepted 4 January 2024)

Impurity generation mechanisms including RF sheath sputtering and heating from fast electrons were explored in LHW sustained plasmas on TST-2 spherical tokamak. Molybdenum impurity was measured with a high-resolution spectrometer and the heating effect on a molybdenum target plate was estimated with a fast camera system. The LHW power modulation experiment indicates that the RF sheath sputtering dominated impurity generation from the antenna limiters (molybdenum) under the current plasma parameters. In addition, the target plate insertion experiment shows that molybdenum atoms were released from the target when heated by fast electrons accelerated by LHW. Although the heating effect was negligible for the antenna limiters, it could become significant under higher plasma parameters or during longer pulses.

Keywords: lower hybrid current drive, impurity, RF sheath, fast electron

DOI: 10.1585/pfr.19.1402010

1. Introduction

Spherical tokamaks (STs) are expected to achieve nuclear fusion economically and efficiently due to the compact configuration and high β [1]. However, the configuration limits the space for a central solenoid. Therefore, non-inductive current drive methods including radio frequency (RF) wave injection have been actively studied on STs. Lower hybrid wave (LHW), which is one of the RF waves, has been investigated on traditional tokamaks, such as JT-60 [2], JET [3], TORE SUPRA [4], and EAST [5]. The results show its high efficiency in plasma heating and plasma current ramp-up. The applicability of LHW on STs is still under research. In TST-2, various launching conditions for LHW have been explored using capacitively coupled comb-line (CCC) antennas, which utilize capacitive coupling between neighboring elements to achieve high directionality, low refractivity, and convenient feeding [6–8]. Thus, understanding the characteristics of CCC antennas is of particular importance for future devices, and the RF sheath effect is one of the topics. RF rectified potential, namely a time-averaged increase in sheath potential, enhances the acceleration of ions in the rectified sheath width and the sputtering on the antenna surface and limiters [9, 10]. The erosion of the antenna surface is crucial for steady-state operation [11–13]. Meanwhile, the released high-Z impurities can dissipate plasma power and deteriorate current drive efficiency. Therefore, it is essential to experimentally evaluate the importance of RF sheath sputtering on CCC antennas. In this experiment, it was confirmed for the first time on a CCC antenna with spectroscopic diagnostics.

In plasmas sustained by LHW, electrons are accelerated almost in parallel to magnetic field lines through electron Landau damping. The electron velocity distribution can become highly anisotropic, and fast electrons, which are important components carrying the plasma current, are formed during the acceleration. According to the fast electron transport model [14], orbit expansions of fast electrons may induce energy deposition on limiters. If the local temperature on limiters exceeds the melting point, a substantial quantity of impurities may be generated. Consequently, heating from fast electrons can be a critical concern for antenna limiters. In earlier studies, it was observed that fast electrons generated within the scrape-off layer (SOL) were responsible for depositing heat onto components near the antennas [15, 16]. However, in this research, the heating was found on a target plate far from the antennas. The majority of fast electrons that hit the target had an energy level exceeding 50 keV, as indicated by hard X-ray (HXR) measurements. This energy level is significantly higher than that of the fast electrons generated in the SOL, as shown in Ref. [16]. Hence, it is more likely that these electrons are associated with suprathermal electrons in the core plasma.

This paper is organized as follows. In Sec. 2, the experimental setup for the high-resolution spectrometer and the fast camera system is given. Section 3 presents the LHW power modulation experiment results, focusing mainly on the RF sheath sputtering. In Sec. 4, the heating from fast electrons is discussed, and results from temperature reconstruction, impurity measurements, and HXR measurements are compared.

author's e-mail: tian@fusion.k.u-tokyo.ac.jp

2. Experimental Setup

In TST-2, molybdenum limiters are used to protect the outer-midplane [6], top [7], and outer-off-midplane [8] antennas. In recent LHW experiments, MoI emission lines at 390.3 nm, 386.4 nm, 379.8 nm, and 313.3 nm were observed with a high-resolution spectrometer (FWHM ~ 0.02 nm). MoI at 379.8 nm was measured to investigate the molybdenum generation mechanisms because of the strongest intensity among the observed lines. Most of the measurements on limiters were taken through chord 1 at tangential radius $R_{\rm tan}$ = 450 mm as shown in Fig. 1. Note that the plasma major and minor radii are less than 360 mm and 230 mm [17]. Furthermore, a Mo target plate was inserted into the outboard SOL in some discharges to examine its interaction with fast electrons. The target is placed far from the antennas, where the RF amplitude is low, thus minimizing the RF sheath effect at the target. It can be moved along the major radius, and measurements presented in this paper were taken when the target tip was positioned at $R_{\rm target}$ = 570 mm, where a maximum emission was observed. Note that the outboard last closed flux surface (LCFS) is usually located around R = 560 mm, and the limiters are located at R = 585 mm. Additionally, the target's rotatability enables varying the poloidal projection area of the fast electron flux, which is almost perpendicular to the poloidal plane. Measurements of the target were taken through chord 2 as shown in Fig. 1.

In estimating the target's temperature, a fast camera system was utilized, employing an IR filter (> 715 nm) and a high frame rate setting. The influence of plasma light became negligible when compared to the heated target. Subsequently, the target was considered a gray body. A tungsten filament which is located at the same distance in the plasma experiments and has a relatively large flat area of 5 mm × 20 mm was used to establish the relationship between filament temperatures and pixel intensities of the fast camera. Note that both molybdenum and tungsten have similar black body radiation emissivities. The filament temperatures under different consumed power were estimated by analyzing their emission spectra with Planck's law. To reduce errors during temperature estimation, particularly for lower temperatures, the consumed power of the filament was fitted to the temperatures using the Stefan-Boltzmann law with heat conduction correction [18]. The obtained relation then converted pixel intensities to temperatures.

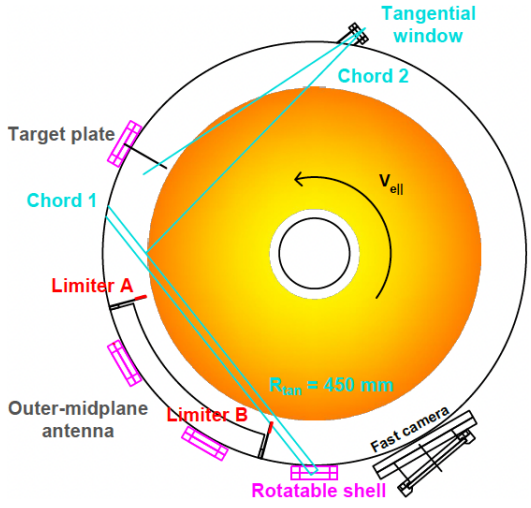

Fig. 1 Observation chords of the high-resolution spectrometer under a top view of TST-2.

3. LHW Power Modulation

Figure 2 shows the typical waveforms of a discharge where the antenna was switched from the outer-midplane antenna to the top antenna at t = 45 ms. Simultaneously, the plasma current and the line-averaged density were maintained around 10 kA and 1.5×10^{17} m^{-3}, respectively. Figure 2 (e) shows the intensity of MoI measured at chord 1, and the difference before and after the switching indicates the strong dependence of molybdenum generation on LHW injection. Similar behavior is often observed in CuI emission lines, which is seen as a good indicator of RF sheath sputtering in TST-2, as the antenna elements are coated by copper. A 50 kW power modulation experiment was then conducted with 2 ms power-on and 2 ms power-off phases as shown in Fig. 3. The measured intensities were processed by a conditional averaging technique, namely accumulated according to power modulation cycles, to enhance the signal-to-noise ratio as shown in Fig. 4. Both CuI and MoI (chord 1) show rapid responses to the power modulation, which is consistent with the expectation for RF sheath sputtering. The typical rising times (10% to 90% magnitude) were 0.18 ms and 0.2 ms for MoI and

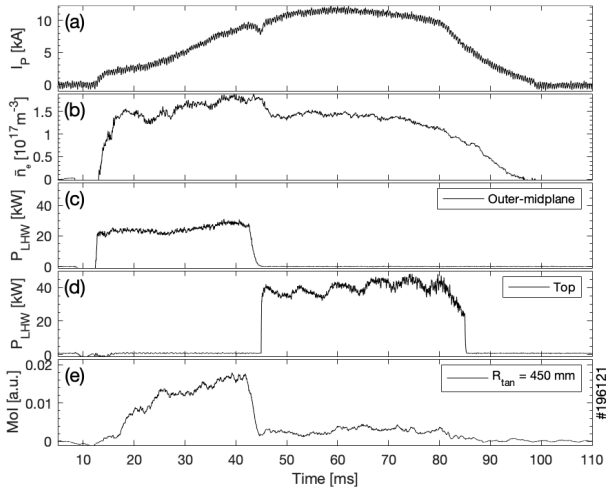

Fig. 2 Waveforms of plasma current I_p (a), line-averaged density $\overline{n_e}$ (b), LHW power $P_{\rm LHW}$ from the outer-midplane antenna (c), $P_{\rm LHW}$ from the top antenna (d), and MoI emission (e) during the antenna switching experiment.

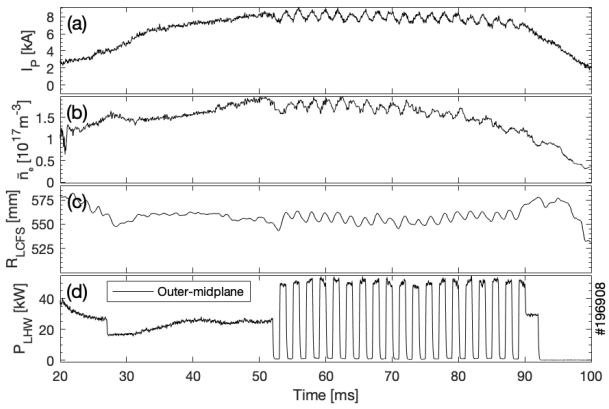

Fig. 3 Waveforms of I_p (a), $\overline{n_e}$ (b), the radial position of outboard LCFS R_{LCFS} (c), and P_{LHW} from the outer-midplane antenna (d) during LHW power modulation experiment.

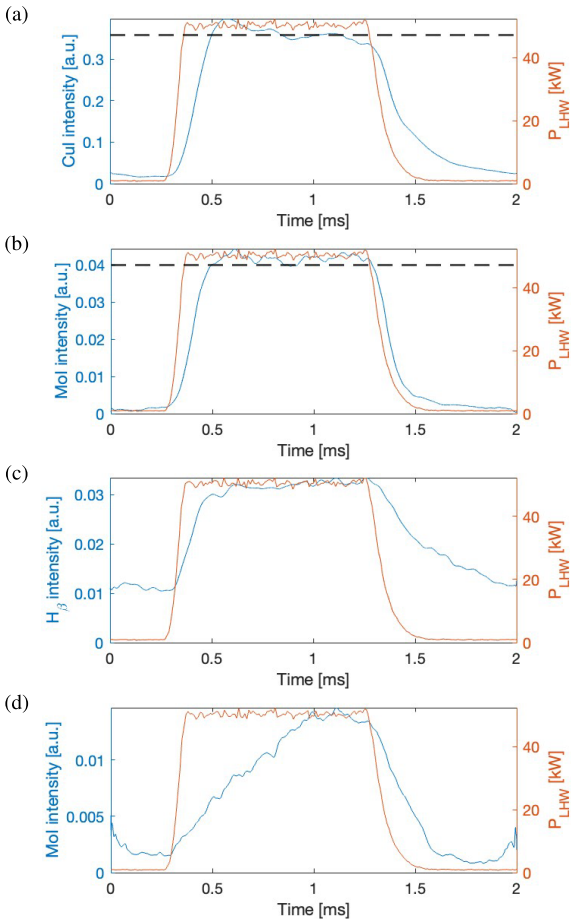

Fig. 4 RF power modulation waveform and corresponding CuI (chord 1) emission (a), MoI (chord 1) emission (b), H_β (chord 1) emission (c), and MoI (chord 2) emission (d) from the target after subtracting the background (i.e., the emission without the target insertion).

CuI, respectively. Note that time delays exist between the measured intensity and the power pulse, and are 0.12 ms and 0.14 ms for MoI and CuI, respectively. The time delay is defined as the time difference between amplitude saturation (90% magnitude). In principle, the RF sheath effect responds almost instantaneously to changes in the RF field amplitude, which is proportional to the square root of the RF power. However, the impurity emission was measured via an observation chord, and a certain amount of time is required for released particles to travel and saturate the chord, resulting in a noticeable delay.

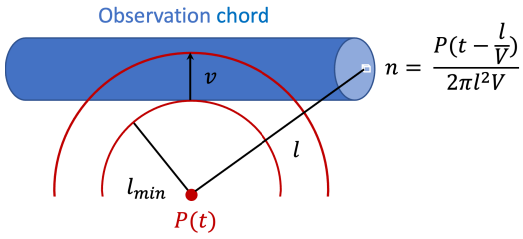

Fig. 5 Impurity density inside the observation chord is contributed by the past source with emission rate P.

Theoretical order estimations of the response time scales for the RF sheath effect are as follows. A point particle source releasing impurities in a half-sphere, as shown in Fig. 5, is considered. The emission rate P is assumed to be proportional to the LHW power. The density n of released impurities inside the observation chord at time t is contributed by the past source as $n = \frac{P(t-l/V)}{2\pi l^2 V}$, where l denotes the distance to the particle source, and V represents the velocity of particles. After reaching maximum LHW power, the emission rate P becomes constant, and the delay is reflected by the variation in impurity density n. Therefore, the time scales lie between the traveling time of the minimum and maximum l. The electric field amplitude near strap 1, with an injection power of 50 kW, was estimated to be 1.1×10^5 V/m based on Fig. 4 in Ref. [19], where the electric field amplitude is shown for 1 W. The sheath potential at strap 1 was calculated to be 280 V using equations in Ref. [20], considering a typical Langmuir probe measurement $n_e = 1 \times 10^{16}$ m^{-3} [21] and a Thomson scattering measurement $T_e = 50$ eV [22] at the edge. TRIM.SP, a Monte Carlo program based on the binary collision approximation, calculates the energy of sputtered atoms [23]. Simulation results by TRIM.SP with various projectiles and sputtered materials are summarized in Ref. [24]. The average energies of sputtered molybdenum and copper atoms, with normal incidence, were found to be 4.5 eV ($\sim$ 3000 m/s) from limiter B and 5.1 eV ($\sim$ 3900 m/s) from strap 1, respectively. Consequently, the time scales for MoI and CuI are 0 to 0.3 ms and 0.01 to 0.24 ms, respectively. Here, l is estimated from the geometrical arrangement of the antenna, the limiter B, and the viewing chord 1. The experimental time delays are consistent with the above estimation. However, the estimated velocity of copper is greater than that of molybdenum, while CuI exhibits a longer delay time compared to MoI in the experiment. The reason for this will be discussed in the next paragraph.

The time scale of spectral line emissions, including excitation and relaxation, is generally at a level of nanoseconds, which will not affect the estimation results. However, it should be noted that antenna power decays from strap 1 (next to limiter B) to strap 13 (next to limiter A) as shown by Fig. 5.3 in Ref. [25]. Since the power is proportional to the square of the RF field amplitude, the RF sheath effect also decays with the distance from limiter B. In this case, the Debye sheath of potential 160 V gradually dominates over the RF sheath, considering the same temperature and density at the edge. The energy of incident particles decreases with the potential drop, leading to a reduction in both the energy and sputtering yield of the resulting sputtered particles. The measured line intensity essentially results from combining point sources representing each strap or limiter. The contribution of each source point to the average velocity can be determined by weighting it according to its respective sputtering yield. Here, the average velocity refers to the average velocity of all released particles of the same impurity. For molybdenum and copper, the sputtering yield dependence on the energy of incident particles is quite different [26]. Molybdenum's sputtering yield at limiter B is about 10 times greater than that at limiter A, and copper's sputtering yield remains almost constant among antenna straps. Such difference causes a different reduction in the average velocities compared to the case considering only strap 1 or limiter B. As a result, the reduced average velocities are about 2900 m/s and 3500 m/s for molybdenum and copper, respectively. The larger reduction in copper's average velocity is due to a higher weight assigned to the straps with lower energy of sputtered particles. This partly explains the longer delay time of CuI compared to MoI in the experiment. Another contributing factor is the variation in l among different source points. However, explaining the variation in l requires a complete reconstruction of the emission process, which will not be addressed in this paper. Additionally, measured CuI exhibits a longer decay time at the power-off phase compared with the rising time at the power-on phase, which is insignificant in MoI (chord 1). This is probably due to self-sputtering [27], as the antenna surface (coated by copper) is significantly larger than that of the limiters, leading to a higher probability of self-sputtering.

Apart from the fast response attributed to the RF sheath effect, H_β emission (Fig. 4 (c)) shows a baseline (i.e., offset) component and a long decay time during the power-off phase, indicating a relatively slow response to the modulation. The release of hydrogen atoms is caused by knocking from charge exchange neutrals and ions in the SOL, which indirectly depends on the LHW power. The energy of incident particles is around the ion temperature of about 10 eV, as determined by Doppler spectroscopy. Such energy is insufficient to generate copper or molybdenum impurities at a level comparable to RF sheath sputtering. In addition, the MoI from the target measured at chord 2 is shown in Fig. 4 (d), having the slowest response during the power-on phase among measured scenarios. This is probably because the production rate of heating-released particles increases with time. As a source of heating, we consider fast electrons, which are accelerated by LHW and enter the SOL [14]. This scenario is discussed in the next section with other experimental results. On the other hand, the sputtering-released particles have a relatively stable production rate under a specific sputtering condition. The occurrence of sputtering or any change in sputtering condition can be reflected by reaching maximum emission intensity in a much shorter time compared to heating, as shown by the power-on phases in Fig. 4. During the power-off phase, the response in Fig. 4 (d) is relatively fast, suggesting that the quenching (heat dissipation) of heated regions was fast. This is similar to the behavior of electron thermal spikes produced by energetic electron beams, and the melting of samples is often observed in transmission electron microscope experiments [28]. Thermal spikes refer to spatially localized increases in temperature produced by the energetic radiation on matter [29]. The localized heat deposition to form thermal spikes is almost instantaneous, causing a large temperature gradient in the surrounding area, and the heat dissipation follows classical thermal conduction. Therefore, expecting a fast quenching of electron thermal spikes during the power-off phase is reasonable. Notice that during the power-on phase, continuous beams of fast electrons hit the target, and the number of generated thermal spikes increases over time, as indicated by the slow rising time.

4. Heating from Fast Electrons

Additional evidence of target heating from fast electrons will be presented in this section. The monotonic increase in MoI intensity contributed by the target became evident with unmodulated RF power, as shown in Fig. 6 (e), where the background was contributed by molybdenum limiters without target insertion. Note that the monotonic increase appears from around 50 ms, which is qualitatively consistent with the heating-release scenario, where a certain temperature threshold exists. The threshold does not necessarily mean that a section of the target reaches the melting point, but rather an overall increase in the target's temperature, which enhances the generation of thermal spikes and results in a detectable difference in the impurity level. Therefore, both the monotonic increase and the delayed appearance are consistent with the heating-release scenario qualitatively. The heating from fast electrons was also captured through a fast camera system, and the target configuration is shown in Fig. 7. The most intense heating effect was often observed just before the LHW power turned off, and the target started to cool down while plasma still existed for more than 20 ms. The whole process of cooling down is longer than 200 ms after the termination of plasma. The temperature distribution on the target is shown in Fig. 8 for cases of differ-

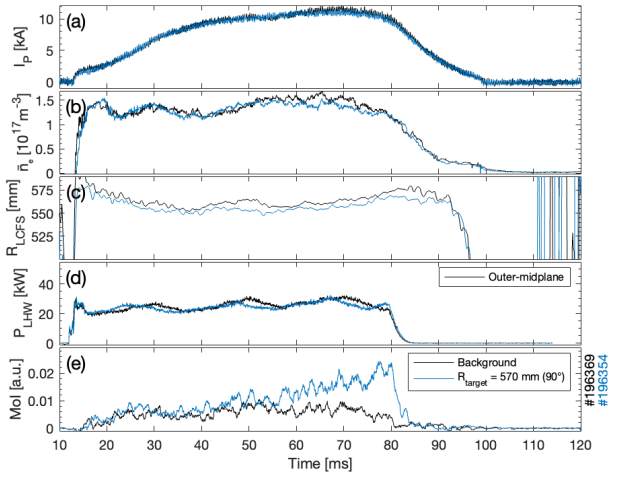

Fig. 6 Waveforms of I_p (a), $\overline{n_e}$ (b), R_{LCFS} (c), and P_{LHW} from the outer-midplane antenna (d) and MoI emission with (light blue) and without (black) target insertion (e) during unmodulated RF experiments.

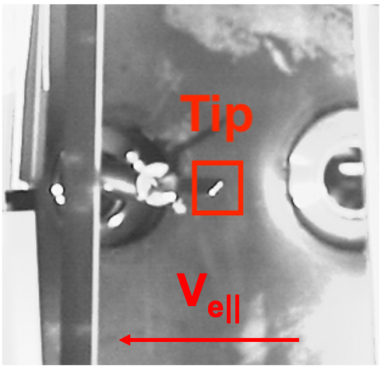

Fig. 7 Photograph of target tip (1 mm × 10 mm) at 45°. The photograph was taken by the same fast camera system without plasma and with another illumination light source.

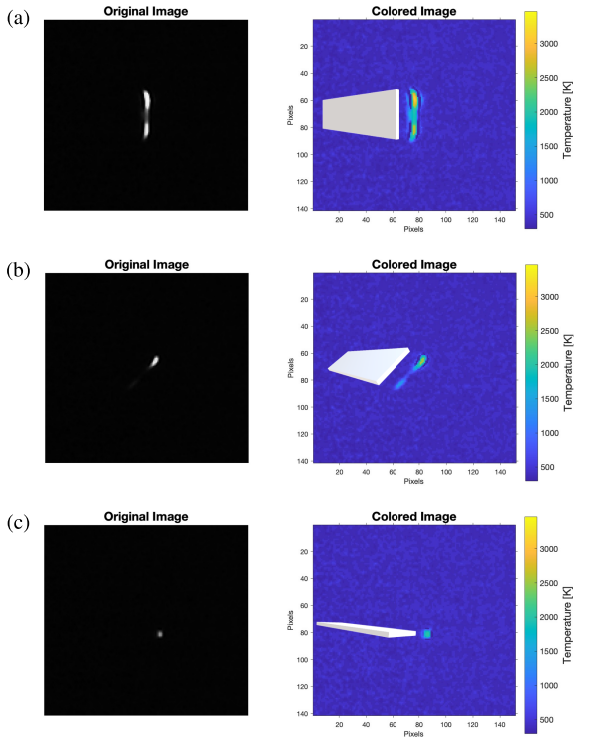

Fig. 8 Reconstructed temperature distributions on the target when R_{target} = 570 mm and the target angles were 90° (a), 45° (b), and 0° (c). Target alignments are shown by white rectangles.

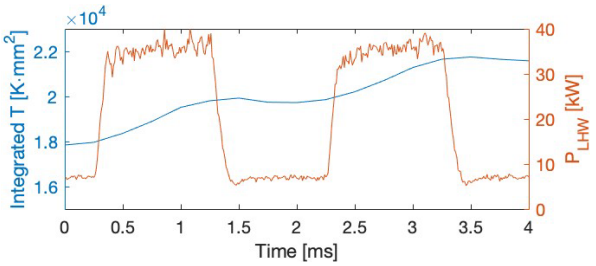

Fig. 9 Integrating temperatures over bright areas on the target during RF power modulation experiment.

ent target angles at the moment of highest temperature. Note that the size corresponding to one pixel on the target is about 0.27 mm × 0.27 mm, which means that the fast camera's resolution is not capable of directly observing thermal spikes, for which we expect a much finer scale. Although the observed highest temperature of 3200 K exceeded molybdenum's melting point of 2900 K, no slowdown of the temperature increase due to the latent heat was observed, suggesting that the temperature error is over 300 K. The temperature distribution reveals that the heating effect on the target always occurs from the right side, which faces fast electrons. This happens regardless of the target's angle, indicating that fast electrons serve as the heating source. Meanwhile, only the tip region was found to be heated during experiments, which means heating power was deposited on a narrow region on the side of the target.

Hereafter, the heat load is interpreted by integrating temperatures over the bright area pixels on the target. A similar experiment as described in Sec. 3 was conducted to examine the response of the heat load to the power modulation, and the accumulated result is shown in Fig. 9. The integrated temperature increases during the power-on phase similar to Fig. 4 (d), but the response during the power-off phase is slow. This is because the temperature change for integrated temperature is governed by macroscopic heat conduction, where the temperature gradient is overall smaller than localized electron thermal spikes, which are responsible for molybdenum generation.

The rotation angle dependence of the target is compared between normalized total energy of HXR, integrated temperature, and MoI intensity as shown in Fig. 10, where

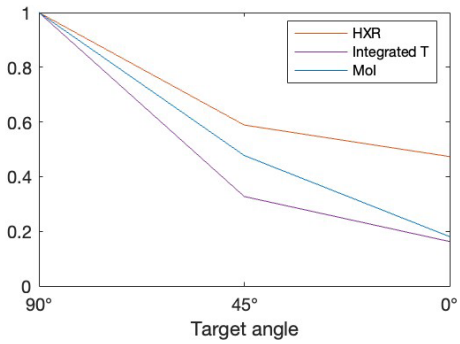

Fig. 10 Comparison between normalized total energy of HXR, integrated temperature, and MoI intensity at different target angles.

the background (without target) is subtracted for MoI measurement, and it was negligible for HXR and fast camera measurement. The HXR detector was located at the tangential window (Fig. 1), aiming at the side of the target. HXR energy, MoI intensity, and the integrated temperature show the highest values when the target angle is 90°, while they show the lowest values at 0°. These behaviors are qualitatively consistent with the scenario where the power deposition and the resultant three quantities arise from the fast electrons hitting the target, and the power is proportional to the projection area of fast electrons on the target. However, since the change of geometry could potentially change the heat flux distribution on the side of the target and the boundary condition of heat conduction, which means that the three quantities are nonlinear functions of the deposited power, quantitative discussion on the angle dependence becomes difficult.

5. Conclusions

Impurity generation mechanisms were investigated using a high-resolution spectrometer and a fast camera system in plasmas sustained by LHW. At the plasma parameters of $I_p \sim 10\,\mathrm{kA}$, $\overline{n_e} \sim 1.5{\times}10^{17}\,\mathrm{m}^{-3}$, and $P_{LHW} \sim 50\,\mathrm{kW}$, the molybdenum impurity was primarily found to be generated through RF sheath sputtering on the antenna limiters. The highest RF sheath potential reached approximately 280 V compared to the Debye sheath of potential 160 V. The impurity response under RF power modulation was consistent with experiments. This is the first quantitative evaluation of the RF sheath effect on a CCC antenna. To further understand the RF sheath effect on CCC antennas, a parametric study is necessary, e.g., P_{LHW} dependence of sheath quantities. We would like to leave it as a future task. Furthermore, a heating effect and impurity release were observed on a molybdenum target plate inserted in the outboard SOL. The heat is expected to be deposited on the target by orbit expansions of fast electrons formed in the core plasma. The modulation of RF power indicates that electron thermal spikes are probably responsible for the generation of molybdenum impurities through the heating of the target. Temperature distributions (right-hand side in Fig. 8) reveal that only a narrow region on the side of the target received heating power from fast electrons. The rotation angle dependence of integrated temperature and MoI intensity shows that the maximum heat load on the target was received at an angle of 90°, while the least heat load was at 0°. This trend aligns with the deposited energy of fast electrons on the side of the target, as measured through HXR detectors. Therefore, it is reasonable to expect that heating from fast electrons could become a more serious problem in longer pulse experiments or with improved plasma parameters.

Acknowledgments

This work was supported by JSPS KAKENHI Grant Numbers 22K03573, 18K13524, and 21226021, by NIFS Collaboration Research Programs NIFS22KIPP007 and NIFS20KUTR155, and by Japan/US Cooperation in Fusion Research and Development.

[1] Y-K. Peng and D. Strickler, Nucl. Fusion **26**, 769 (1986).
[2] K. Ushigusa *et al.*, Nucl. Fusion **29**, 1052 (1989).
[3] D. Moreau and C. Gormezano, Plasma Phys. Control. Fusion **33**, 1621 (1991).
[4] G. Tonon, Plasma Phys. Control. Fusion **35**, A105 (1993).
[5] F. Liu *et al.*, Nucl. Fusion **55**, 123022 (2015).
[6] Y. Takase *et al.*, Nucl. Fusion **53**, 063006 (2013).
[7] T. Shinya *et al.*, Nucl. Fusion **57**, 036006 (2017).
[8] Y. Ko *et al.*, Nucl. Fusion **63**, 126015 (2023).
[9] H. Kohno *et al.*, Phys. Plasmas **22**, 072504 (2015); erratum: **23**, 089901 (2016).
[10] J. Myra, J. Plasma Phys. **87**, 905870504 (2021).
[11] J. Noterdaeme and G. Oost, Plasma Phys. Control. Fusion **35**, 1481 (1993).
[12] V. Bobkov *et al.*, Nucl. Mater. Energy **18**, 131 (2019).
[13] L. Colas *et al.*, Nucl. Fusion **62**, 016014 (2022).
[14] A. Ejiri *et al.*, Plasma Fusion Res. **17**, 1402037 (2022).
[15] P. Jacquet *et al.*, Nucl. Fusion **51**, 103018 (2011).
[16] V. Fuchs *et al.*, Phys. Plasmas **3**, 4023 (1996).
[17] Y. Takase *et al.*, Nucl. Fusion **41**, 1543 (2001).
[18] M. Carlà, Am. J. Phys. **81**, 512 (2013).
[19] S. Yajima *et al.*, Nucl. Fusion **59**, 066004 (2019).
[20] P. Chabert and N. Braithwaite, *Physics of Radio-Frequency Plasmas* (Cambridge University Press, Cambridge, 2011) p. 113.
[21] J. Rice *et al.*, Plasma Fusion Res. **15**, 2402009 (2020).
[22] H. Togashi *et al.*, Plasma Fusion Res. **10**, 1202082 (2015).
[23] J. Biersack and W. Eckstein, Appl. Phys. A **34**, 73 (1984).
[24] W. Eckstein, *Calculated Sputtering, Reflection and Range Values (IPP 9/132)* (Max-Planck-Institut fär Plasmaphysik, Garching, 2002).
[25] T. Shinya, *Non-Inductive Plasma Current Ramp-up on the TST-2 Spherical Tokamak Using the Lower Hybrid Wave* (Doctoral dissertation, The University of Tokyo, 2015).
[26] Y. Yamamura and H. Tawara, At. Data Nucl. Data Tables **62**, 149 (1996).
[27] D. D'Ippolito *et al.*, Plasma Phys. Control. Fusion **33**, 607 (1991).
[28] T. Yokota *et al.*, Phys. Rev. Lett. **91**, 265504 (2003).
[29] G.H. Vineyard, Rad. Effects **29**, 245 (1976).